



HAL
open science

Surface Modification of Brass via Ultrashort Pulsed Direct Laser Interference Patterning and Its Effect on Bacteria-Substrate Interaction

Aisha Saddiqa Ahmed, Daniel Wyn Müller, Stephanie Bruyere, Anne Holtsch, Frank Müller, Jenifer Barrirero, Kristina Brix, Sylvie Migot, Ralf Kautenburger, Karin Jacobs, et al.

► **To cite this version:**

Aisha Saddiqa Ahmed, Daniel Wyn Müller, Stephanie Bruyere, Anne Holtsch, Frank Müller, et al.. Surface Modification of Brass via Ultrashort Pulsed Direct Laser Interference Patterning and Its Effect on Bacteria-Substrate Interaction. ACS Applied Materials & Interfaces, 2023, 15 (30), pp.36908-36921. 10.1021/acscami.3c04801 . hal-04185599

HAL Id: hal-04185599

<https://hal.science/hal-04185599>

Submitted on 23 Aug 2023

HAL is a multi-disciplinary open access archive for the deposit and dissemination of scientific research documents, whether they are published or not. The documents may come from teaching and research institutions in France or abroad, or from public or private research centers.

L'archive ouverte pluridisciplinaire **HAL**, est destinée au dépôt et à la diffusion de documents scientifiques de niveau recherche, publiés ou non, émanant des établissements d'enseignement et de recherche français ou étrangers, des laboratoires publics ou privés.

Surface modification of brass via ultrashort pulsed direct laser interference patterning and its effect on bacteria-substrate interaction

Aisha Saddiqa Ahmed^{a,b}, Daniel Wyn Müller^a, Stephanie Bruyere^b, Anne Holtsch^c, Frank Müller^c, Jenifer Barrirero^a, Kristina Brix^d, Sylvie Migot^b, Ralf Kautenburger^d, Karin Jacobs^c, Jean-François Pierson^b, Frank Mücklich^a*

^a Chair of Functional Materials, Department of Material Science and Engineering, Saarland University, 66123 Saarbrücken, Germany

^b Université de Lorraine, CNRS, IJL, F-54000 Nancy, France

^c Experimental Physics and Center for Biophysics, Saarland University, 66123 Saarbrücken, Germany

^d Department of Inorganic Solid-State Chemistry, Elemental Analysis, Saarland University, 66123 Saarbrücken, Germany

Keywords

ultrashort pulsed direct laser patterning, femtosecond pulse duration, brass, zinc oxide, copper oxides, nanoscale chemical modification, nanoscale heat-affected zone, antibacterial

Abstract

In recent decades, antibiotic resistance has become a crucial challenge for human health. One potential solution to this problem is the use of antibacterial surfaces, i.e., copper and copper alloys. This study investigates the antibacterial properties of brass that underwent topographic surface functionalization via ultrashort pulsed direct laser interference patterning. Periodic line-like patterns in the scale range of single bacterial cells were created on brass with a 37% zinc content to enhance the contact area for rod-shaped *Escherichia coli*. Although, the topography facilitates attachment of bacteria to the surface, reduced killing rates for *E. coli* are observed. In parallel, a high-resolution methodical approach was employed to explore the impact of laser induced topographical and chemical modifications on the antibacterial properties. The findings reveal the underlying role of the chemical modification concerning the antimicrobial efficiency of the Cu-based alloy within the superficial layers of a few hundred nanometres. Overall, this study provides valuable insight into the effect of alloy composition on targeted laser processing for antimicrobial Cu-surfaces, which facilitates the thorough development and optimization of the process concerning antimicrobial applications.

1 Introduction

Rapidly increasing infectious diseases remain a major social problem, and the threat of antibiotic resistance is a significant concern.¹ However, alternative strategies such as the use of antimicrobial surfaces offer a promising solution to effectively inhibit the growth and spread of harmful microorganisms.²⁻⁴ Inspired by nature's morphological blueprints, researchers are constantly investigating new techniques to harness their beneficial properties.⁵ The nanopillars on cicada wings are a primary example of a naturally occurring antibacterial effect owing to the surface structures.⁶ On the contrary, the hydrophobic behaviour of the

Lotus leaf is a result of micro- and nanostructures as well as their surface chemistry, which gives them a self-cleaning function.⁷

A variety of techniques have been developed for the functionalization of surfaces to alter their characteristics. These include chemical or/and topographical alterations realized via methods like nanoparticle fabrication, micro and nano-structuring, and creating photocatalytic surfaces.^{3,8,9} Direct laser interference patterning (DLIP) technology¹⁰ has been utilized for over a decade to modify surfaces down to the nanoscale. DLIP in combination with ultrashort pulse (USP) durations has proven to provide attainable precise nanostructures.¹¹⁻¹³ This is attributed to the curtailed melting zone by the virtue of shorter pulse durations.¹⁴ As whole, the scope of DLIP application is defined remarkably wide including functions such as tribology,¹⁵⁻¹⁷ electrical conductivity,¹⁸ antibacterial properties,^{3,19} and wettability.^{20,21} Moreover, various materials ranging from metals to polymers, depending on the application, have been modified via laser technology.²²⁻²⁶

Metals like copper, copper alloys, cadmium, and silver have been the focus of investigation for their naturally occurring antibacterial properties.^{3,4,22,27-29} Moreover, metal oxides like zinc oxide and titanium oxide, which show antibacterial activity upon exposure to ultraviolet light, are also being investigated.^{8,30} In the case of pure copper, surface modification via ultrashort pulsed direct laser interference patterning (USP-DLIP) was shown to further improve the already pronounced inherent antibacterial properties.^{3,31,32} This involves an increased Cu-sensitivity alongside improved bacterial contact conditions.³ The antimicrobial effect of Cu surface is directly related to the quantitative release of cytotoxic Cu-ions, which are known to deteriorate both bacteria and viruses by several modes of action e.g., targeting the cell wall, proteins, and DNA.^{31,33} Here, the presence of copper oxides can impact the antibacterial properties: Excessive cupric oxide (CuO) was shown to reduce antibacterial efficiency, whereas, for predominant cuprous oxide (Cu₂O) composition, it is improved.³⁴

Despite the advantageous antibacterial properties of copper, its limited mechanical properties, including low hardness and strength yield, restrict its widespread use e.g., as antibacterial surfaces in public and private infrastructure to prevent the transmission of harmful microorganisms. In this case, alloying represents a powerful approach to optimize the properties according to the desired application.

For this study, a commercially available copper alloy with 37 % zinc content (brass, CuZn37) is chosen. The zinc in brass adds to the hardness and durability of the material.³⁷ The aim is to use USP-DLIP to fabricate periodic line-like structures in the scale range of single bacteria cells, firstly to understand the laser-material interaction and secondly to test the impact of USP-DLIP processing on antibacterial efficiency. Various characterisation methods are employed to determine the effect of the alloying on the degree of surface modification, which include scanning electron microscopy (SEM), high-resolution grazing incidence X-ray diffraction (GI-XRD), scanning transmission electron microscopy along with energy dispersive X-rays spectroscopy (STEM-EDS), atom probe tomography (APT), electron diffraction (Selected area electron diffraction, SAED or Fast Fourier Transform image, FFT) via transmission electron microscopy (TEM), X-ray photoelectron spectroscopy (XPS), scanning tunnel microscopy and spectroscopy (STM and STS) and Raman spectroscopy. The structured surfaces are then tested for their antibacterial activity against *Escherichia coli* WT K12 (BW25113) to understand the correlation with surface modifications achieved via USP-DLIP.

2 Materials and methods

2.1 Materials and preparation

The commercially available brass with 37 wt.-% zinc (M37; *Wieland*), CuZn37, was chosen for this work. It should be noted that for Cu-Zn alloys the composition given in wt.-% differs

only marginally from the composition given in at.-%. Additionally, 99.95 % pure copper (*Wieland*), and stainless steel (*Brio*) were utilized as references. The samples were acquired in the form of a sheet with a thickness of 1 mm and were then cut to a dimension of approx. $25 \times 10 \text{ mm}^2$. Since a smooth initial surface topography is required for the subsequent laser process, the sample surfaces were prepared metallographically. Prior to that, microhardness of brass was measured with *Struers Dura Scan 50 microhardness tester*, which is required to determine the polishing parameters, as the high copper content in the samples can present a challenge during preparation due to its softness. The Vickers hardness (HV 0.1) value for CuZn37 was recorded at 107 ± 9 . This value is almost double that of pure copper, yet low compared to steel. For that reason and to avoid any big deformations, the process was started with fine grinding. First, SiC paper with a grain size of $15 \mu\text{m}$ was utilized on a manual Tegrapol system (*Struers*) to remove the uppermost layer of deformations. Next, the surfaces were polished with an automated TegraPol system (*Struers*) to finally obtain a mirror-quality finish. This was executed in a total of three steps i.e., $6 \mu\text{m}$, $3 \mu\text{m}$, and $1 \mu\text{m}$ grain size, each using the respective all-in-one diamond solutions (*Struers*).

2.2 Ultrashort Pulsed Direct laser interference patterning (USP-DLIP)

USP-DLIP technology was utilized to produce line-like structures with a periodicity of $3 \mu\text{m}$ on the brass surface. For the surface modification, a Ti:sapphire Spitfire laser system (*Spectra Physics*) with ultrashort laser pulses (pulse duration of $t_p = 100 \text{ fs}$, full width at half maximum - FWHM) was utilized. The centred wavelength λ was 800 nm . The optical setup was chosen as described in Müller *et al.*³⁸ The setup consists of a beam diameter aperture, a wave plate, a diffractive optical element (DOE), a mask and a focusing lens system with a 100 mm focal length. First, the laser beam passes through an aperture, which adjusts the beam diameter and transforms the intensity profile from Gaussian to near Top Hat shape. The beam is then forwarded to a wave plate that changes the polarisation angle of the beam

perpendicular to the orientation of fabricated patterns. Subsequently, the DOE splits the beam into two coherent partial beams. These are then diverted by a lens to finally interfere on the sample surface. These create maxima and minima of intensity in the focal spot leading to the formation of line-like periodic structures via ablative processes. Looking at the superimposed profile in cross-section, a wave-like intensity distribution profile with broad valleys and narrow peaks emerges as described in Müller *et al.*³⁸ The periodicity of these line-like structures is linked to the incident angle of single laser beam on the sample surface. This interference setup hereby is similar to the Fresnel mirror setup,³⁹ which describes the periodicity p according to equation (1).

$$p = \frac{\lambda}{2 * \tan \alpha} \quad (1)$$

here λ is the wavelength of a laser beam and α is the incident angle of a single partial beam. As the surface is irradiated with a laser beam, the energy is first absorbed by the electrons and then transferred onto the lattice until a thermal equilibrium is achieved.¹⁵ The electron-lattice relaxation time hereby is in the range of a few picoseconds,⁴⁰ whereby laser material interaction within and below this range is described involving a Two-Temperature model.⁴¹⁻⁴³ In the case of femtosecond pulses, the relaxation time is considerably longer than the pulse duration. Therefore, it is highly improbable to realize a thermal equilibrium in the lattice. As a result, a direct solid to vapor/plasma phase transformation is observed, instead.⁴⁴ Depending on the applied fluence regime very thin melting depths are expected alongside ablation via spallation or phase explosion.^{13,45} Due to averted thermal diffusion within this time scale, very high temperatures and pressure are experienced in the thermal response of irradiated matter. This results in thermal and mechanical lattice distortion of the material. Due to which the uppermost surface undergoes topographical as well as chemical modifications. This includes remelting, rapid solidification and redeposition of previously ablated matter in the shape of oxidic particles.²² In this work, a total of 24 samples were structured. 12 of the laser structured

samples were then etched to remove the process induced oxides. For that purpose, samples were emerged in 5 % citric acid, then placed in an ultrasonic bath for 2 min and finally cleaned with ethanol. For any further experiments, the samples were aged at least for three weeks to ensure stable and reproducible wettability conditions.³

2.3 Surface characterization

The topography of the samples was observed with confocal laser scanning microscopy (CLSM, *LEXT OLS4100 3D Measuring Laser Microscope by Olympus*). A quantitative phase analysis was performed via high-resolution grazing incidence X-ray diffraction (GI-XRD, Cu K_a source with a wavelength of 1.54 Å at 1° grazing angle, *PANalytical X'Pert PRO-MPD*).

Scanning electron microscopy (SEM, *Helios NanoLab 600™, FEI*) was used to acquire images in secondary electron contrast mode. An acceleration voltage of 5 kV at a current of 1.4 nA was applied and the sample was tilted at 45° to improve visualization of topographic pattern features. Subsequently, cross-sections of the line-like structures were examined by the means of SEM/FIB (Focused Ion Beam) Lamellas (perpendicular to the lines) that have been prepared on the sample surface before lift out and mounting on a TEM-grit for further Ion-beam thinning to reach e-beam transparency. These are analysed via scanning transmission electron microscopy (STEM) also including energy dispersive X-ray spectroscopy (STEM-EDS, *JEOL ARM 200F equipped with two Cs correctors*) to determine the chemical composition via mapping and profiling. This characterization was further supplemented by the electron diffraction imaging via transmission electron microscopy.

The surface and subsurface effects of modification were characterized by atom probe tomography (APT). This was accomplished in a *LEAP 3000X HR (CAMECA)* with laser-pulsed mode for the regions with oxides and voltage-pulsed mode for the subsurface composition. All APT measurements were performed at a temperature of about 60 K, repetition rate of 100-200 kHz, pressure lower than 1.33×10^{-8} Pa, and evaporation rate of 2-5

atoms per 1000 pulses. Laser pulsed APT was carried out with a pulse energy of 0.5-0.6 nJ; and voltage measurements with 20 % pulse fraction. The reconstruction and analysis of the datasets was done with the commercial software *IVAS*TM3.6.8 (*CAMECA*). Compositions were calculated by applying a peak decomposition algorithm included in the analysis software. As the name explains, this algorithm decomposes overlapping peaks based on the natural isotopic ratios. In the present case, the most important overlap occurs in the mass-to-charge spectrum at 32 [Da] due to the overlap of the most abundant peaks of O_2^{+1} and Zn^{+2} . Due to this overlap it is not possible to construct concentration profiles across the different oxides in the reconstructions. APT specimens were prepared in a FIB/SEM dual-beam workstation (*Helios NanoLab 600*TM, *FEI*) by the lift-out technique described by Thompson *et al.*⁴⁶ The analysed surface was covered by a chromium capping deposited by physical vapor deposition (PVD) to ensure the preservation of the region of interest. After lift-out and thinning of the specimens, a low energy milling at 2 kV was performed to minimize gallium induced damage.

Additionally, scanning tunnelling microscopy and spectroscopy (STM/STS, VT-STM by *Scienta Omicron*) was utilized to further map the surface topography and investigate the electronic structure of the surface. Finally, the oxide characterization was done with Raman Spectroscopy (*Horiba Jobin, HRLab* with a 532 nm laser) as well as X-Ray Photoelectron Spectroscopy XPS, *Vacuum Generators ESCA MKII*, non-monochromatic Al- K_{α} radiation, $\eta\omega=1486.6$ eV, normal emission, data analysis according to Ref.²²).

2.4 Wet plating

The antibacterial activity of brass surfaces was tested via the wet plating method.⁴⁷ Bacteria of the strain *E. coli* WT K12 (BW25113) were implemented in the wet plating and were stored at 4 °C. The bacteria culture preparation was performed as described in Müller *et al* and Luo *et al.*^{3,4} The strain was grown overnight aerobically in Lysogeny broth (LB) medium at 37 °C in a water bath with a speed of 220 rpm. The next day, the bacterial culture was taken

out and centrifuged at $5000 \times g$ to separate the stationary cells. The centrifugation process was repeated three times with phosphate-buffered saline (PBS) using the same parameters. Finally, the stationary cells were resuspended in PBS to prepare the bacterial suspension. 40 μL of the bacterial suspension was applied on the tested surfaces in the shape of a droplet. The region of contact was defined by a polyvinyl chloride (PVC) ring.³ The test was conducted in an environment of saturated humidity at room temperature for a duration of 30, 60, and 120 min. At the end of each respective time, two samples of 5 μL of the suspension were retreated from the droplet after repetitive pipetting. The first was then serially diluted in PBS and finally spread on LB agar plates. The plates were stored in an incubator at 37 °C for 24 h. Finally, the surviving colony-forming units (CFU) were counted to enumerate the viable bacteria of the sampled suspension. As a first reference, the original CFU/mL value of the suspension was chosen. As further references, mirror-polished surfaces of pure copper and stainless steel were tested simultaneously. The second 5 μL of the droplet was diluted in to 600-fold of 0.1 % HNO_3 to determine the Cu-ion release during the exposure time, which is measured with inductively coupled plasma mass spectrometry (ICP-MS, *Agilent 8900 ICP-QQQ*).

2.4.1 Solution info

Phosphate-buffered saline (PBS) was prepared using $\text{NaH}_2\text{PO}_4 \cdot \text{H}_2\text{O}$ (*Merck*, Germany, final concentration 0.01 M), NaCl (*VWR*, Germany, final concentration 0.14 M) and pure water for analysis, and its pH value was adjusted to 7.4 by adding NaOH . It was autoclaved after preparation for sterilization.

3 Results and Discussion

3.1 Topography of the USP-DLIP structures

Line-like structures with the periodicity of 3 μm were fabricated on CuZn37 using a fluence of 0.98 J/cm² with a total number of 9 pulses ($N=9$). According to CLSM measurements, the aimed periodicity of $3.0 \pm 0.1 \mu\text{m}$, and a depth of $1.30 \pm 0.14 \mu\text{m}$ was achieved. Figure 1 a shows the surface after laser treatment also referred to as the as-processed samples. As expected, the SEM micrographs exhibit line-like surface patterns comprising of narrow peaks and broad valleys.

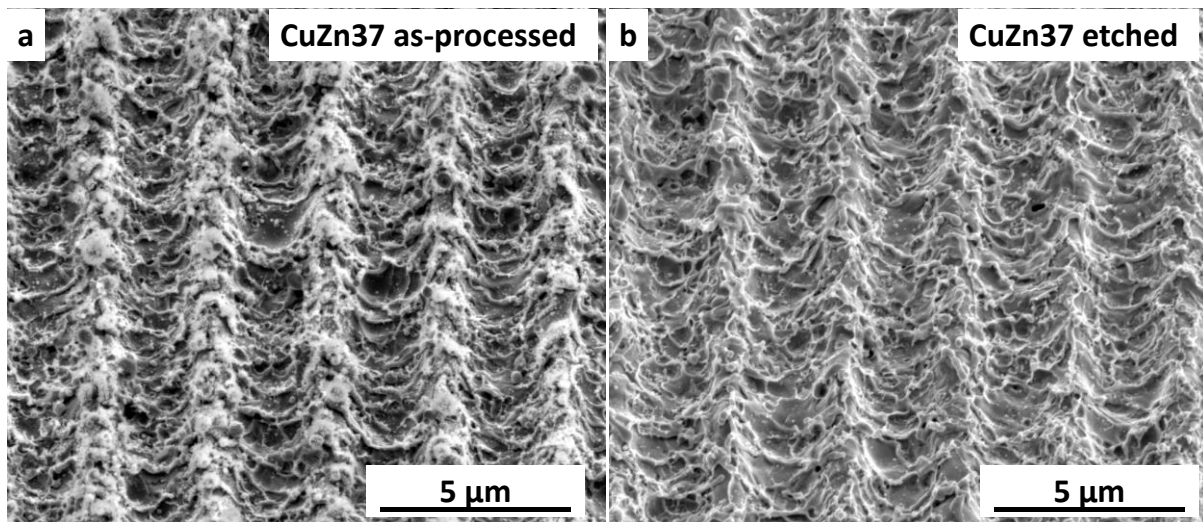


Figure 1 SEM-Topography: 3 μm periodic line-like structure with USP-DLIP on CuZn37 (a) as-processed and (b) after etching with citric acid (The images were obtained at a tilt angle of 45°).

The aim here is to allow the bacteria to settle well within the valleys and have contact area to the substrate regardless of the direction of placement. Furthermore, the deep valleys provide additional contact for the bacteria that accumulate on the monolayer, and overall, a larger contact area is achieved. Apart from that a layer of flake-like sub-structures is observed that indicates the formation of oxides consequent to laser processing, as also shown by Müller *et al.* (2021).³ The presence of oxides plays a vital role in altering the crucial parameters of

antibacterial properties i.e., Cu-ion release on contact and the adhesion of bacteria. Firstly, depending on the oxidation state of pure copper, the release of Cu-ions is affected.⁴ And secondly, the adhesion of bacterial droplets is impaired by the reduced wettability due to the topographical construct of the oxides but also due to the accumulation of carbon species during the aging process i.e., carbon oxides, hydrocarbons, etc.

In the case of pure copper, it has been demonstrated that removing this layer can further alter the antibacterial efficacy.³ To examine the effect of oxidation on brass, the structured samples were etched with citric acid to remove the possible oxides. Figure 1 b shows an efficient removal of the sub-structures, making the surface morphology underneath more visible. As a result, the attention is drawn towards the actual geometry of the fabricated structures with a peak-valley ratio of 1:2.3 and hence, a 2.3-fold increase in the actual surface area. Likewise, the concave shape of valleys is revealed, which provides favourable conditions for bacteria to settle in the valley. The SEM micrographs also show nano-roughness along the lines suggesting melting and redeposition together with the ablation. Ablation occurs as a result of locally high confined stresses in the surface, which are produced via high temperature during laser irradiation.^{48,49} The observed surface morphology points towards ablation predominantly in the phase explosion regime involving the ejection of the molten matter.⁵⁰ Parallel to ablation, the melted matter also creates multi-pulse ripples.⁵¹ Another prominent feature is the small round nano-particles mostly on the peaks formed due to the redeposition of exploded melted particles.^{52,53} These further add to the depth of the crater. Overall, the morphology of the structures corresponds to the ones in previous studies.^{3,22}

3.2 Morphological and chemical surface modification

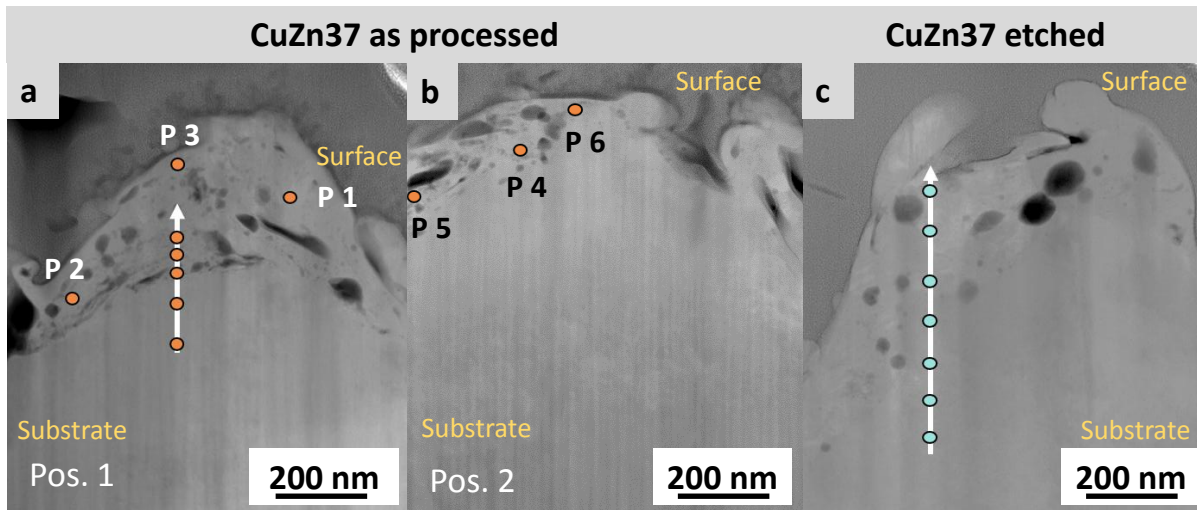


Figure 2: STEM high angle annular dark field images of CuZn37 lamellas displaying the cross section of the peaks from. (a, b) as-processed and (c) etched with EDS-line scan (points on the arrow) as well as individual scan points.

Lamellas were lifted out perpendicular to the line-like structures (see Figure S1 in SI) from both structured samples and analysed with STEM-EDS. The same procedure was repeated with numerous measurements of peaks and valleys of the structures to achieve the results (see Figure 2 a and b).

The high angle annular dark field-TEM images in Figure 2 reveal the nanoscale surface morphology of the surface with clear redeposition of the molten matter on the peaks. Since the fabrication is done via a multi-pulse laser irradiation, the multiple piling of redeposited matter is observed,⁵⁴ which in this case leads to the formation of pores within the layers as shown in Figure 2.

Table 1: STEM-EDS results of CuZn37. This includes the line scan and point scans (P 1-6) from Figure 2 (a, b) on the as-processed and line scan from Figure 2 (c) on the etched sample.

Distance from the surface [nm]	at.-%		
	Cu	Zn	O
422	62.1	35.3	2.6
314	63.1	35.2	1.8

			260	52.8	37.4	9.8	
			206	50.4	37.1	12.5	
			179	41.0	39.4	19.6	
		<i>P 1</i>	125	52.9	43.7	3.4	
		<i>P 2</i>	102	59.5	36.9	3.6	
		<i>P 3</i>	23	52.1	42.1	5.8	
		<i>pos. 2</i>	<i>P 4</i>	90	53.1	42.2	4.7
			<i>P 5</i>	50	52.0	41.2	6.8
			<i>P 6</i>	15	34.8	59.8	5.4
<i>etched</i>		<i>Distance from the surface [nm]</i>	<i>at.-%</i>				
			<i>Cu</i>	<i>Zn</i>	<i>O</i>		
		606	63.4	34.3	2.3		
		505	64.3	35.0	0.7		
		404	63.7	33.6	2.7		
		303	62.1	35.1	2.8		
		202	61.3	36.4	2.3		
		101	58.6	37.0	4.4		
	10	44.4	39.2	16.4			

The results of EDS line scans for the as-processed sample (Table 1) show a drastic modification of the chemical composition for CuZn37 approx. 250 nm from the surface, which also includes the layers of redeposited matter. The uppermost scan point of the line scan on Position 1 (see Figure 2 a and Table 1) shows that the surface has a reduced amount of copper (approx. 41 at.-%) in comparison to the bulk. On the contrary, zinc (39 at.-%) and oxygen (up to ~20 at.-%) are detected in abundance, which suggests the formation of oxide rich regions. At the same time, the Cu-Zn ratio of 2:3 (excluding oxygen) was recorded at a few points that suggest the diffusion of zinc towards the outer surface. It can be explained by the exceptionally high thermal energy as well as the kinetic energy in the near surface range caused by laser irradiation, which enables the diffusion of copper and zinc atoms in the subsurface. This indicates the occurrence of the Kirkendall effect.⁵⁵ Concurrently, additional mobility for the atoms can be anticipated in the redeposited matter during remelting, which is experienced due to the multi-pulse laser irradiation.

The results on position 2 (see Figure 2 b), however, exhibit a non-gradual alteration of Cu-Zn-O ratio from the bulk to the surface. For that reason, few point scans were carried out on both positions to investigate the discrepancies. Table 1 contains the results of point scans on

position 1 (P1 - 3) and position 2 (P4 – 6) confirming varying distribution ratios in the modified surface area. Here, few points with lower oxygen at.-% have a Cu-Zn ratio that corresponds to the stoichiometry of β phase of brass.^{56,57}

After etching, the uppermost layer still has increased amounts of zinc and oxygen (see Figure 2 c and Table 1). However, the chemical modification is only observed for ~100 nm from the surface. Furthermore, the variation of the Cu-Zn ratio for points with less oxygen is not that significant. Overall, the total variation of chemical composition after etching suggests that a layer consisting of zinc rich phase with oxidic components was removed. This indicates that the uppermost surface consists mostly of zinc richer oxide areas, as it also agrees with the oxidation prone nature of zinc in comparison to copper.⁵⁸ The varying distribution ratios recorded for the modified area are further investigated in the next sections.

3.3 Determination of local elemental distribution

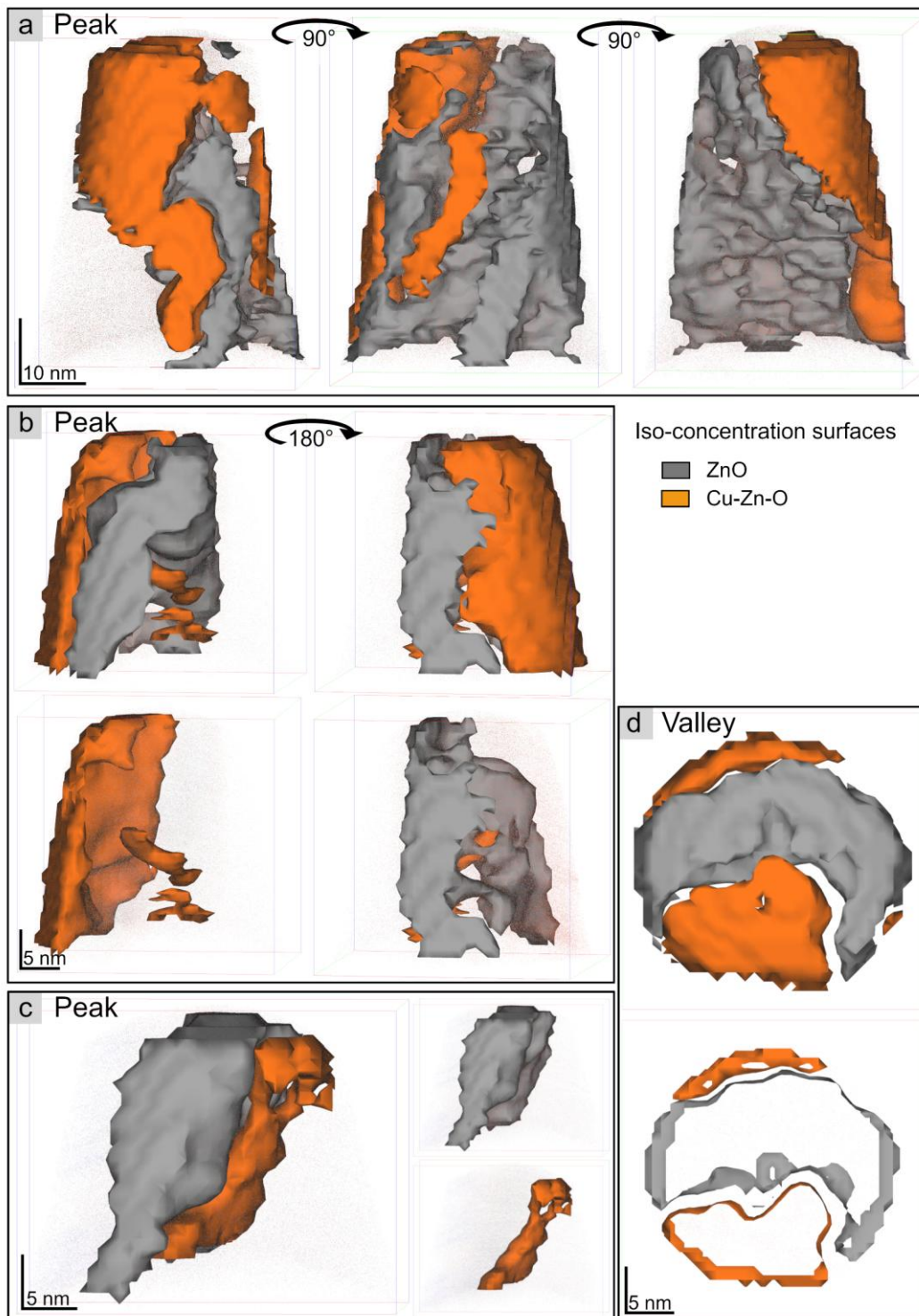


Figure 3: Atom probe tomography (APT) reconstructions of the oxidized surface in sample CuZn37 as-processed [Iso-concentration values for gray surfaces 55-57 at.-% Zn and for orange surfaces 20-33 at.-% Cu depending on the composition of the Cu-Zn-O region]. (a, b,

c) peak and (d) valley of the line-like structure with their respective chemical composition in Table 2.

APT is utilized to investigate the three-dimensional local distribution of elements in CuZn37 as-processed. Specimens from the peak and valley of the line-like structures were prepared and analysed. The volumes reconstructed have a diameter of ~30 nm and a depth between 20 and 50 nm and give an image of the surface oxidation of the sample.

The results confirm an inhomogeneous distribution of Zn, Cu, and O. All specimens depicting the oxidized surface show two regions with distinctive compositions. To determine the composition of each of these regions, the atoms corresponding to each of them were selected by the construction of iso-concentration surfaces for Zn and Cu and exporting the atoms inside (see Figure 3).⁵⁹ In all cases the iso-concentration values were chosen so that they enveloped intertwined volumes rich in Zn and rich in Cu separately.

Figure 3 shows four APT reconstructions giving an overview of the oxides' distribution. Besides the superficial measurements shown in Figure 3, two extra measurements were performed below the oxidized layer to measure the subsurface composition. Figure 3 summarizes the composition of each of the oxidized regions in Figure 3 and the subsurface region.

Table 2: APT results of CuZn37 as-processed

Figure 3		at.-%		
		Cu	Zn	O
Peak	a	5.2 ± 0.1	54.0 ± 0.2	40.8 ± 0.1
		54.9 ± 0.3	34.3 ± 0.3	10.8 ± 0.1
Peak	b	6.4 ± 0.1	46.1 ± 0.3	47.4 ± 0.1
		50.6 ± 0.2	19.8 ± 0.2	29.6 ± 0.1
Peak	c	4.9 ± 0.1	49.7 ± 0.3	45.4 ± 0.1
		33.8 ± 0.6	43.0 ± 0.8	23.3 ± 0.3
Valley	d	2.8 ± 0.2	52.5 ± 0.6	44.6 ± 0.1
		36.4 ± 0.5	35.5 ± 0.4	28.1 ± 0.1
Sub surface		58.3 ± 0.1	41.2 ± 0.1	0.6 ± 0.1
		55.9 ± 0.2	42.6 ± 0.2	1.6 ± 0.1

The Zn-rich oxide (grey in Figure 3) shows a stoichiometry near ZnO with Zn:O ratios ranging from 1 to 1.3 and a low concentration of Cu of 2 - 5 at.-%. On the other side, the complementary regions (orange in Figure 3) show varying contents of the three elements Cu-Zn-O. Similar chemical compositions were also detected using STEM-EDS on CuZn37 as-processed (see Table 1). These compositions indicate the formation of a Cu-Zn-O transitional region. Two recent papers ^{60,61} discuss the formation of Cu-Zn-O nanoparticles and layers with varying compositions and discuss the diffusion of Cu atoms upon annealing. In this work, high temperature and stress are induced on the sample surface by USP-DLIP, followed by a rapid cooling that promotes the formation of metastable phases alongside crystallographic defects.

The results show the diffusion of elements along with ablation and redeposition through laser irradiation. The subsequent chemical modification at subsurface levels indicates that the thermal diffusion length is greater than the ablation depth in the valley. Moreover, there is an absorption of certain amounts of laser energy on the peaks. Although these regions are exposed to the minima of the interference modulated intensity profile, the absorption cannot be entirely excluded. This indicates that a nanoscale heat affected zone (HAZ) is given due to residual thermal energy. This energy is sufficient to increase the mobility of elements, which presumably leads to oxygen penetration to a depth of a few hundred nanometres and forms the Cu-Zn-O regions. Moreover, the redeposited matter is also exposed to the residual thermal energy due to multi-pulse laser irradiation. This leads to high kinetic energy⁵⁴ exposing the redeposited matter to additional oxygen diffusion. Parallel to that, outward diffusion of Zn from this region can be anticipated, which is supported by the Kirkendall effect⁵⁵ as well as the oxide prone nature of zinc. Therefore, the formation of Zn-rich oxide phase is observed. It should also be noted that in a thermodynamically stable state, the whole diffusion should lead to the formation of stable segregated phases. However, in this case, the pulse duration is ultrashort. Therefore, a rapid cooling of the surface most probably hinders the formation of

stable phases. Hence, the occurrence of metastable Cu-Zn-O transitional regions is observed. The discrepancies recorded in the Cu-Zn-O ratio of these regions are probably due to variations in the amount of oxygen that diffuses into the HAZ as well as into the redeposited matter. Another factor could be the kinetic energy of the atoms, which can vary depending on the energy absorbed in the different regions. All these factors together affect the diffusion of all elements and hence the chemical composition.

Furthermore, the subsurface of the valley is analysed (see Figure 3) and the recorded chemical compositions confirm the presence of the intermetallic β phase of brass. This indicates the formation of the β phase most credibly through the rapid cooling of the α phase in the heat affected zone as well as redeposited material. All these findings summarized, propose nanoscale segregated regions consisting mainly of zinc rich oxide phase with either insignificant or lower amount of Cu suggesting the existence of Zn-O and transitional Cu-Zn-O regions, respectively. Furthermore, the regions with insignificant amount of oxygen suggest the existence of the intermetallic β phase.

3.4 Microstructural characterization

The annular dark field STEM images (Figure 2) show a contrast in the modified area for both as-processed and etched samples. This suggests segregation of diverse regions and variation in microstructure due to laser structuring. To investigate this, selected area electron diffraction (SAED) patterns were taken and indexed with the corresponding interplanar spacing (d -spacing) values.

Figure 4 displays the TEM micrographs of CuZn37 as-processed and its respective electron diffraction patterns. The first pattern was taken in the bulk area I (Figure 4 a), which corresponds to the α -brass (220) diffraction spot and zone axis $\langle 101 \rangle$. The respective SAED pattern is typical for a monocrystalline cubic structure.⁶² This additionally indicates that the measurement was carried out in a single grain implying a grain size of larger than 150 nm.

However, the next patterns in the modified area (area II (c) and area III (d)) incorporate discrete spots revealing a polycrystalline structure⁶³, which suggests grains with a smaller size. Here, area II represents β -brass (110), (211), and (222) diffraction spots, and area III represents the Cu_2O (111), (200), and (222) diffraction spots.

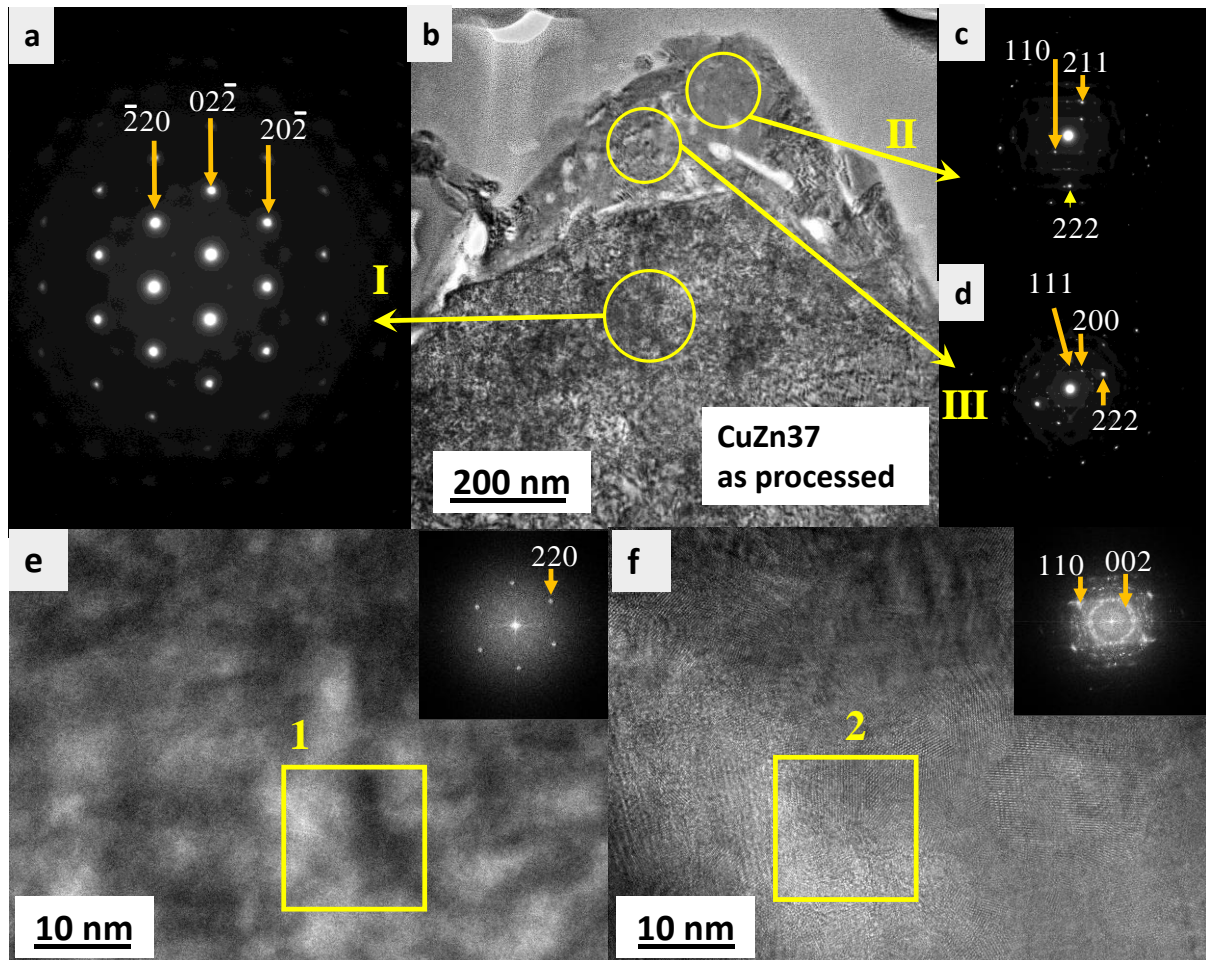


Figure 4: TEM-electron diffraction and images on CuZn37 as-processed. (a, c, d) SAED patterns taken from (b). (e, f) HR-TEM images of the modified area with their respective binned FFT patterns of a selected area (yellow square).

For a detailed understanding, higher resolution (HR) images were collected and evaluated with the Gatan software to acquire the patterns and respective d -spacing values. Figure 4 e shows the result of the bulk region with diffraction spot correspondent to α -brass. An additional measurement is carried out in the visually lighter region of the modified surface (see Figure 4 f) and the resulting appearance of the pattern indicates the presence of a

polycrystalline structure. This pattern can be assigned to the ZnO (002) and (110) diffraction spots. Next, CuZn37 etched is taken under observation and similar results are obtained. The respective SAED patterns (see Figure S2) alongside a detailed discussion are presented in the supporting information. Overall, the position of α -brass in the bulk and β -brass on the surface correlates with the depth of modified areas observed with STEM-EDS analysis for both samples. The HR-TEM micrographs and their respective FFT patterns show mono- and polycrystalline structures for brass phases suggesting an inhomogeneous grain size distribution. Moreover, the presence of Cu₂O and ZnO is identified.

Similar results were achieved from all the above characterization methods. Besides the topographical surface modification, USP-DLIP processing has a localised effect on the composition of the alloy itself and leads to the occurrence of the β phase of brass, as suggested by the APT and TEM analysis. Additionally, the formation of zinc and copper oxide phases is proposed.

3.5 Phase analysis with grazing incidence X-ray diffraction (GI-XRD)

GI-XRD analysis was performed to identify the phases present on the structured surface and the results were simultaneously compared to the polished sample. Figure 5 illustrates X-ray diffractograms for all CuZn37 samples. The polished surface (black diffractogram) has peaks at 42°, 49°, 72°, 87.4°, 92.4°, and 113°, which can be attributed to the α phase of brass with 63 wt.-% copper and 37 wt.-% zinc (ICDD:04-003-2952). Simultaneously, additional peaks are observed for both CuZn37 structured samples, of which the peaks at 43.5°, 63°, 78.7°, 95.5°, and 111° can be assigned to the β phase of brass (LPF:558003, ICDD:04-006-6026). Furthermore, the peaks at 36.3° and 63° can be allocated to cuprous oxide (Cu₂O) (ICDD:04-007-9767). It is to be noted, that the position at 63° is an overlap of β -brass (200) at slightly lower and Cu₂O (220) at slightly higher 2θ values. The remaining additional peaks at 40.5°, 45.4°, and 47.1° are recorded for Cu₂O formed under especially high pressure (ICDD: 00-

035-1091),⁶⁴ which are realized during ultrashort laser irradiation⁵⁰. The results indicate a possible oxidation and validate the formation of an intermetallic phase during the laser process.

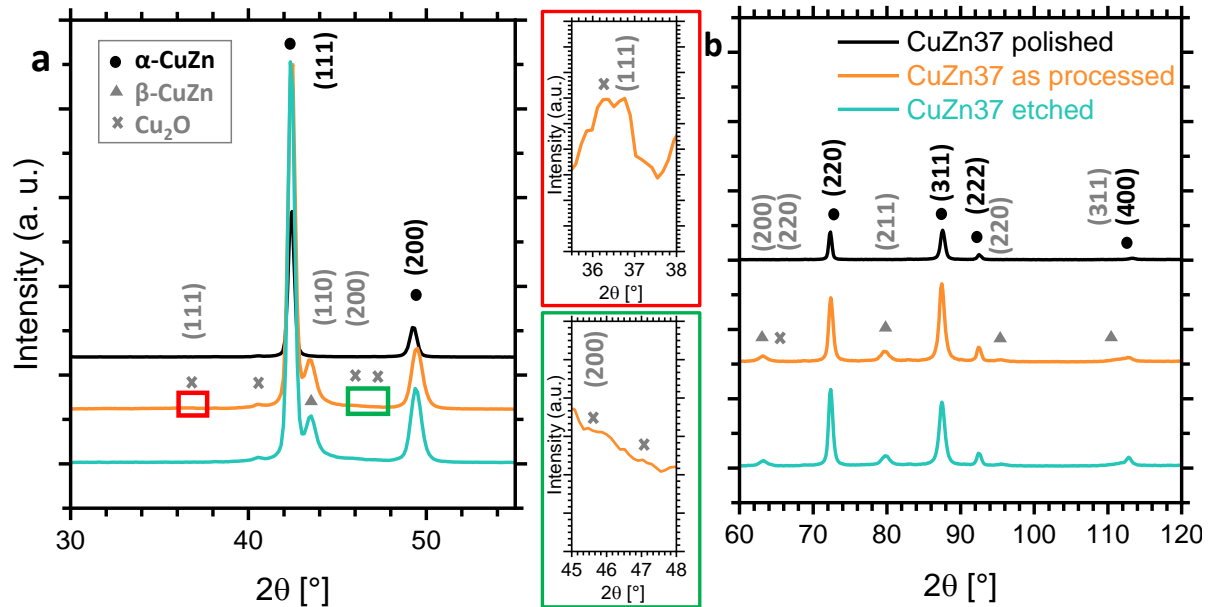


Figure 5: GI-XRD Phase analyses of CuZn37 samples i.e., polished (black), as-processed (orange) and etched (green). 2θ -range: (a) 30° - 55° and (b) 60° - 120°

The formation of the intermetallic phase is entirely dependent on the bulk chemical composition. All the phases that can exist at various temperatures for any given chemical composition are shown in the Cu-Zn phase diagram in Figure S3. It shows that above 30 ± 3 wt.-% of zinc, more than one phase can exist at various temperatures. At 37 wt.-% of zinc, the phase likely to form is the β phase in two modulations depending on the temperature. This is a result of, first, extreme temperatures achieved via high laser power applied for the process. Second, due to the ultrashort pulse duration, rapid cooling of the surface can be anticipated after the laser beam has interacted with the surface. As a result, the intermetallic β phase is formed, as confirmed by the GI-XRD diffractograms. At this stage, the complete identification and verification of the oxide phases present on the surface is still unresolved. The SEM micrographs suggest a successful removal of flake-like sub-structures via etching,

but the XRD- diffractograms show cuprous oxide peaks, which remain unaltered even after etching. This is further analysed and verified in the following sections.

3.6 Identification of oxide phases on the superficial layer

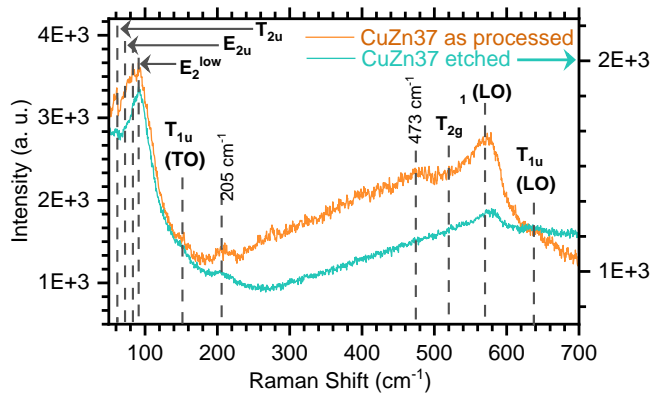


Figure 6: Raman spectra of CuZn37 as-processed (orange) represented by left y-axis and etched (green, right y-axis).

To develop an understanding of the type of oxides, the results were complemented by Raman spectroscopy analysis. Figure 6 illustrates the Raman spectra of CuZn37 samples. Bands are observed at 61, 73, 83, 92, 147, 206, 473, 520, 572, and 643 cm^{-1} for CuZn37 as-processed (orange spectra). All the characteristic bands of ZnO are visible. However, a slight shift to lower values is noted for E_2^{low} (92 cm^{-1}) and LO (572 cm^{-1}) indicating an increase in the quantity of ZnO-defects.⁶⁵ The reason behind the existence of defects is perhaps the suppression of zinc oxide formation. Even though the oxidation of zinc is favoured over copper, there is a potential concurrence between both due to the higher copper content. Besides that, the stress produced at higher temperatures and limited reaction time, in this case, can inhibit the full and thermodynamically stable formation of oxides.⁶⁶ Furthermore, a weak peak is observed at 473 cm^{-1} . A similar band in the range 450-500 cm^{-1} has been reported for a zinc rich zone in an annealed brass sample with higher zinc content.⁶⁷ However, this literature, does not provide an exact value or discussion on the existence of this band. Additionally in the same paper, this peak is not visible for brass samples with lower zinc

content.⁶⁷ Since there is very broad band between 300-600 cm^{-1} with a tilted baseline, the weak characteristic bands of ZnO in this range are most probably suppressed. In addition to that, the silent and IR-active modes of Cu_2O , as well as the T_{2g} band is detected at 516 cm^{-1} . These all results confirm the presence of ZnO and Cu_2O after the laser process. In total, the literature values of all the characteristic bands for the vibrational modes active in Raman as well as in IR and the silent modes for the oxides alongside the results of this paper are stated in Table S1 in the SI.

After etching CuZn37 surface, the intensity of the band is reduced significantly, and the baseline appears to be flatter. Since the intensities of the bands are comparatively higher for the as-processed sample, CuZn37 etched is represented by the right y-axis. The reduced intensities can be attributed to the significant reduction of the intensive LO band of ZnO indicating a substantial loss of zinc oxide. Additionally, the band experiences a shift to a higher value suggesting a decline in ZnO-defects. Moreover, the band at 473 cm^{-1} is no longer visible. All the Cu_2O bands can still be observed, but now at lower Raman shifts. The reduction in intensities of the ZnO and Cu_2O bands for the etched sample suggests a lower oxide amount on the surface in comparison to the as-processed.

The results of Raman spectroscopy validate formation of cuprous and zinc oxide on the brass surface via laser processing. However, after etching the sample, partial removal of zinc oxide is observed.

3.7 Identification of oxide phases at surface and subsurface layer

This section is concerned with the investigation of the subsurface distribution of oxides via XPS analyses combined with surface ablation by Ar^+ -ion etching. The XPS-based elemental depth profiles suggest an increase in the zinc and oxygen concentrations on the laser structured surface. This validates the formation of zinc oxide by laser processing, which

complements the results until now. A detailed discussion alongside the depth profiles is present in Figure S4 in the SI.

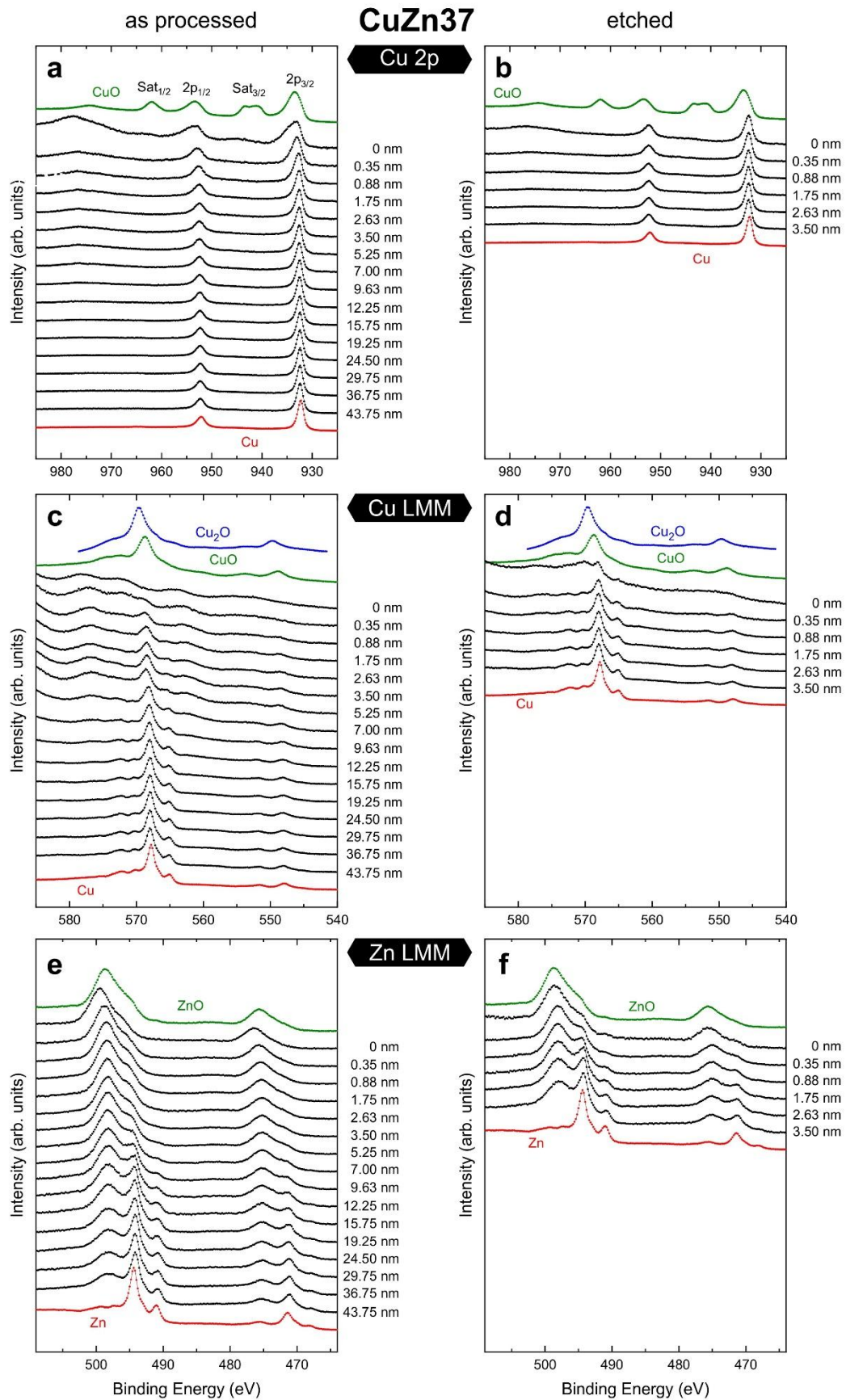


Figure 7: XPS - results of CuZn37 with high resolution spectra of (a, b) Cu 2p, (c, d) Cu LMM (e, f) Zn LMM of as-processed and etched samples.

Besides C (as resulting from adsorbates) the XPS survey spectra indicate only the presence of Cu, Zn, and O. Therefore, XPS detailed spectra were recorded for O 1s, Cu 2p, Zn 2p, Cu LMM, and Zn LMM to reveal the elemental composition of the samples as well as the oxidation state of Cu and Zn. To distinguish Cu, Cu₂O, and CuO, both the Cu 2p_{3/2} spectra, and the Cu LMM spectra are needed. In the Cu 2p spectra CuO can be distinguished from Cu and Cu₂O via the chemical shift to higher binding energies as well as via the characteristic satellite at higher binding energy.⁶⁸⁻⁷² In the Cu LMM spectra, Cu can be distinguished from Cu₂O and CuO mainly via the low binding energy (=high kinetic energy) tail of the L₃M₄₅M₄₅ Auger peak. For ZnO and Zn, the Zn-2p_{3/2} spectra display no difference. However, the Zn-LMM Auger peaks display distinct differences in peak shape as well as in peak position.^{68,73,74}

The Cu 2p_{3/2} spectra of CuZn37 as-processed together with the reference CuO and Cu are plotted in Figure 7 a. For the as provided sample i.e., before Ar⁺-ion etching (0 nm ablation), the spectrum displays a superposition of Cu/Cu₂O and CuO (with the latter being identified via the weak satellite at about 940 – 945 eV). After ablation of approx. 0.35 nm the CuO related features i.e., the satellite as well as the high binding energy shoulder of the 2p_{3/2} peak disappear. This implies that the presence of CuO only applies to the uppermost surface layer. To reveal the distribution of Cu₂O, Figure 7 c shows the Cu LMM Auger spectra in comparison with the spectra for Cu and CuO as probed on reference samples. The spectrum for Cu₂O is taken from Fig. 5 in Ref.⁷⁰ With increasing ablation the Cu LMM spectra in Figure 7 c display a systematic decrease of Cu₂O (as seen by the increasing intensity of the Cu⁰ characteristic L₃M₄₅M₄₅ Auger peak at about 565 eV). At this stage, it is not possible to give a distinct value for the subsurface range with Cu₂O contributions. However, when

comparing with the Cu LMM spectrum of the Cu reference sample in Figure 7 c, the Cu LMM spectra at 9.63 nm or 12.25 nm are very similar to the Cu reference spectrum. Therefore the “thickness” of the Cu₂O layer can be approximated smaller than 10 nm. Whereas CuO (according to the XPS results from Figure 7 a) is mostly distributed on the uppermost layer of the surface.

The Zn LMM spectra (including the spectra from ZnO and Zn reference samples) are represented in Figure 7 e. In contrast to CuO and Cu₂O, the presence of ZnO is not a surface or near subsurface related issue. In the whole range of ablation, i.e., up to approx. 44 nm into the bulk, the Zn LMM spectra display a superposition of the Zn and ZnO reference data. At the surface and in the topmost layers the spectra indicate that the amount of ZnO is much larger than the amount of Zn. However, with each step of ablation the ZnO:Zn ratio decreases, and the presence of Zn starts to dominate at depths between approx. 15 nm and 20 nm. Figure 7 a, c and h give clear evidence that Zn acts as an oxygen scavenger. This is also supported by the O 1s spectra in Figure S5 in the SI. With increasing depth, the O 1s intensity (with the binding energy matching with the O 1s binding energy for ZnO) decreases in the same way as the intensity of the ZnO related contribution of the Zn LMM spectra.

After etching, the Cu 2p spectra in Figure 7 b display no significant contributions of CuO. Even for zero ablation the Cu 2p spectrum displays only marginal contribution of the CuO related satellite i.e., even at the surface, there is nearly no CuO. Concerning the presence of Cu₂O the Cu LMM spectrum at 0 nm (Figure 7 d) shows a superposition of Cu and Cu₂O. Soon after ablation i.e., approx. at 0.35 nm, a significant change in the intensity ratio is observed indicating the presence of mainly pure copper.

The Zn LMM spectra in Figure 7 f show that even after etching there are still contributions of ZnO at the surface as well as in the subsurface range. However, compared to the as-processed CuZn₃₇ sample in Figure 7 c the relative amount of ZnO is strongly decreased. In addition, there is a stronger decrease of ZnO with increasing depth (for example, the Zn LMM

spectrum of CuZn37 etched at about 3.50 nm ablation in Figure 7 f is comparable to the Zn LMM spectrum of CuZn37 as-processed at about 19.25 nm ablation in Figure 7 e). Therefore, etching the CuZn37 sample reduced the thickness of the (mainly) ZnO layer by approx. half an order of magnitude.

Overall, the STEM-EDS, Raman, and XPS results are in good agreement. This is indicated by the presence of cupric, cuprous, and zinc oxide on the surface after structuring with USP-DLIP. All the results indicate a higher amount of zinc oxide than other oxides. The weak intensities of CuO peaks in XPS spectra indicate an occurrence in a remarkably lower quantity. Literature^{67,75} reports that cuprous oxide formation is favoured at higher/increasing temperatures because of the predominant lattice diffusion whereas cupric oxide is a result of grain diffusion at relatively lower temperatures. Thus, the Cu₂O formation can be deeper into the surface, and CuO largely on the outer surface. The etching results suggest a partial removal of zinc oxide and full removal of CuO. On the other hand, it is evident that the Cu₂O formed is stable and is not altered via etching.

3.8 Spatial distribution of metal and oxide phases

Scanning tunnelling microscopy and spectroscopy (STM and STS) measurements were used on all sample surfaces to investigate the spatial distribution of the metal and oxide phases. The STM result in SI Figure S6 exhibits a variation of the profile both perpendicular and parallel to the line-like structures, confirming the periodicity as well as the nano roughness along the valleys, which is consistent with the CLSM results. Furthermore, STS is conducted on the peaks and valleys of the samples to investigate the local density of electron states (LDOS) as a function of electron energy, which in this case is the voltage applied between the sample and the tip. LDOS, hereby, is material dependent and thus directly influences the slope of the $I(V)$ curve. The $I(V)$ curve is divided into two regimes i.e., the ohmic regime (-0.2 to +0.2 V) with a linear behaviour in dependence to the conductivity and

the Fowler-Nordheim regime ($-0.2 < V < +0.2$) with an exponential-like behaviour where the slope depends on the work function of the material.²²

The $I(V)$ curves (averaged over several hundred measurements at various positions) of the peak and valley for both samples are displayed in Figure 8. The curve of CuZn37 as-processed in Figure 8 a shows a significantly lower conductivity at the peak with a nearly flat behaviour at voltages between $-0.5 < V < 0.5$ indicating the presence of a semiconductor phase. This is attributed to a much lower presence of oxide phases with a semiconducting behaviour. Here, the larger band gaps (E_g) and work functions (Φ) of zinc oxide ($E_g: 3.37 \text{ eV}$, $\Phi: 4.7\text{-}5.1 \text{ eV}$)^{76,77} and copper oxides ($E_g: 1.2\text{-}2.2 \text{ eV}$, $\Phi: 5.0\text{-}5.5 \text{ eV}$)²² are responsible for the lower conductivity. At the same time, the valley exhibits an increased conductivity suggesting an enhanced contribution by a conductive metallic phase. This is attributed to the presence of copper and zinc phases with lower work functions ($\Phi(\text{Cu}): 4.5 \text{ eV}$, $\Phi(\text{Zn}): 3.6 \text{ eV}$).^{22,76,77}

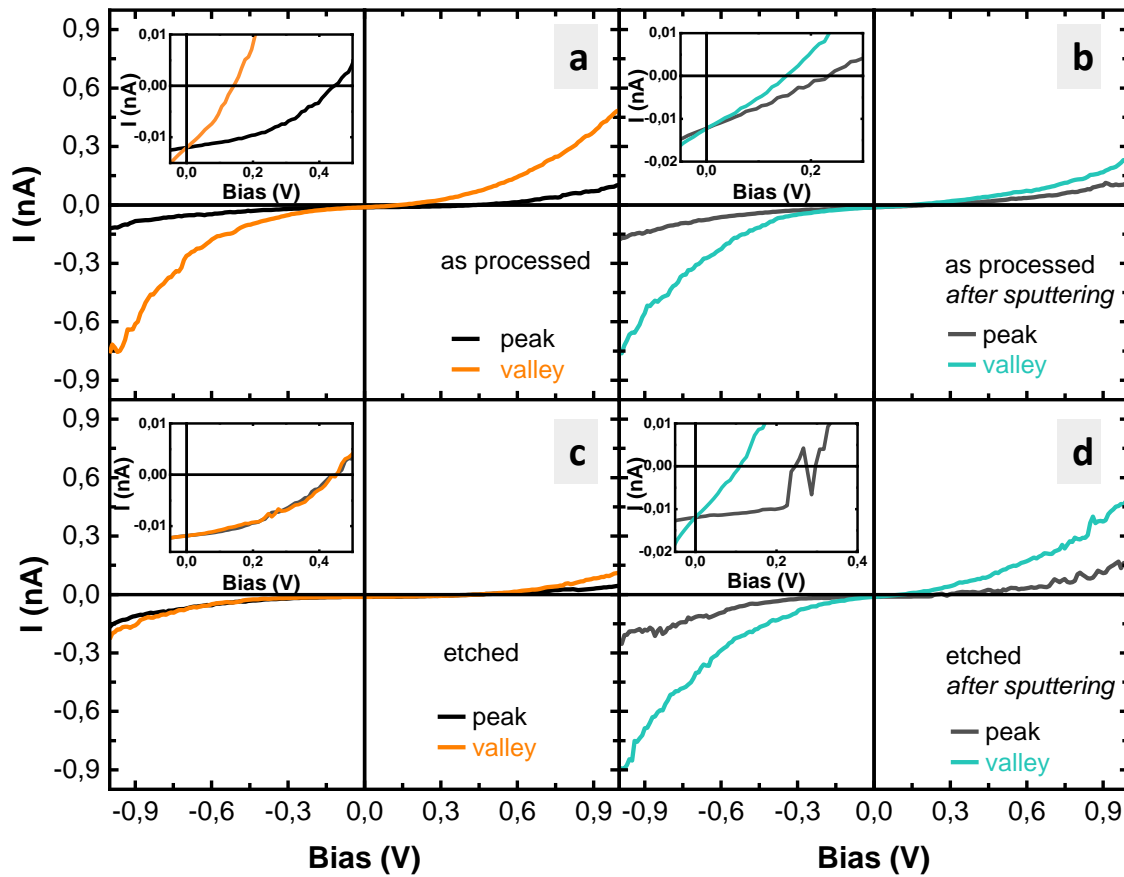


Figure 8: CuZn37 (a) as-processed and (c) etched before Argon sputtering as well as (b) as-processed and (d) etched after argon sputtering.

Additionally, argon ion etching was applied for both surfaces to examine the spatial distribution in the subsurface range. After sputtering (see Figure 8 b), the peak and valley exhibit similar conductivity suggesting a higher concentration of conductive metallic phase alongside the semiconductor oxide phases in relatively lower quantity.

The etched CuZn37 exhibits identical conductivity behaviour for the peak and valley indicating the presence of a semiconductor phase. However, after argon sputtering the subsurface level show an increase in conductivity on the valley confirming the reduction of the oxide phase. Overall, the results reveal the presence of a semiconductor oxide phase on the peaks, which is significantly deeper into the surface. Whereas the valleys indicate the

coexistence of metallic and oxide phases on the uppermost surface as well as the subsurface level for as-processed and etched samples, which is in agreement with the preceding results.

3.9 Antibacterial tests

Contact killing tests were carried out on CuZn37 including USP-DLIP processed surfaces at a pattern periodicity of 3 μm in as-processed and etched surface state. Additionally, mirror-polished Cu and stainless steel were used as topographically smooth and inert reference surfaces. The results were evaluated taking into account the changed contact area due to surface modification and thereby also the altered wettability. On one hand, the patterned surfaces have a 2.3-fold increase in surface area. On the other hand, the wettability changes significantly within the first week after laser structuring, finally stabilizing after 3 weeks of aging. The wetting behaviour changes from hydrophilic in the first week to hydrophobic after at least 3 weeks of aging.²² As a result, when the droplet with the bacterial suspension was placed on the structured sample, it occupied only ~33 % of the PVC-ring area. However, on the etched surface, the wettability is slightly increased, and the droplet covered up to ~47 % of the ring area. Considering all these factors, the surviving CFU/mL over a contact period of 120 min is plotted in Figure 9 a. In the same Figure, the respective Cu-ion releases for 120 min are charted as bars.

Predictably,³ the stainless steel (grey graph) shows nearly no reduction in the CFU-value over the 120 min exposure. Simultaneously, a quick reduction in surviving CFU-value is noted for pure copper (red graph). Proceeding with CuZn37 polished (black graph in Figure 9), a fast reduction in CFU-value for the same exposure time but rather slower than that of pure copper is recorded. This is an expected result due to the lower concentration of copper,^{4,78} which is confirmed by the attenuated Cu-ion release (Figure 9 b). In the as-processed state (orange graph Figure 9), a considerably reduced killing and corresponding copper-ion release rate are observed, which denotes an inadequate antibacterial activity,

despite the increased and improved contact area. This is attributed to chemical alteration of the surface via laser treatment resulting in depleted copper content and therefore, zinc rich phases/regions. While zinc does have a cytotoxic effect on bacterial cells, it is much less pronounced compared to copper. Furthermore, the presence of zinc oxide in these conditions is very stable chemically, making the release of Zn-ions improbable.

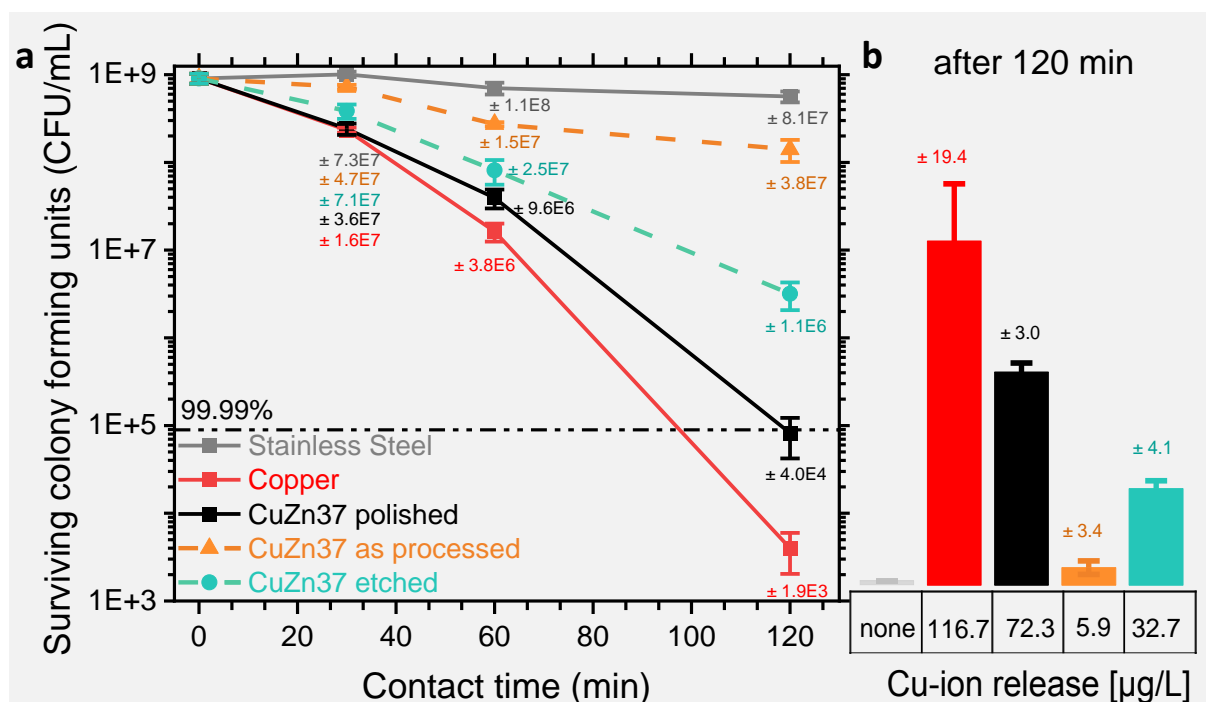


Figure 9: (a) Surviving colony-forming units as results of contact killing experiment with *E. coli* for 30, 60 and 120 min on CuZn37 surface. (b) The respective Cu-ion release values after 120 min of exposure time in form of a bar chart.

After etching, the surface exhibits an improved efficiency (see green graph Figure 9) with an increased Cu-ion release. This is ascribed to the partial removal of zinc rich oxide phases resulting in exposure of certain copper rich metallic or the more stable cuprous oxide phases that are susceptible to corrosion. However, it is not quite sufficient to even reach the level of the polished CuZn37 surface. The comparison between the antibacterial activity of as-processed and etched sample indicate that the higher amount of zinc oxide leads to higher corrosion resistance in wet conditions containing bacteria.

4 Conclusion

The present study investigates the nanoscale surface modification of brass by means of USP-DLIP and sheds light on the mechanisms involved in the alteration of the antibacterial properties. At first, USP-DLIP was employed to create the 3 μm line-like structures. GI-XRD, STEM-EDS, APT, and STM/STS analysis reveal topographical as well as chemical variation as a result of the laser process, which infuses a few hundred nm of depth. The results confirm presence of zinc rich zones and formation of an additional intermetallic β phase on the uppermost surface. Another interesting result observed is the formation of oxides via USP laser processing. The Raman and XPS results confirmed the presence of zinc oxide in abundance, followed by cuprous oxide and cupric oxide in a comparatively low concentration. Additionally, formation of transitional Cu-Zn-O regions is detected. The formation of the metastable phases is most presumably a consequence of the Kirkendall effect in combination with the rapid cooling of the melted and redeposited matter, as it hinders the formation of stable phases. After etching the laser processed samples with citric acid, a partial removal of zinc oxide and a full removal of CuO is observed. Whereas Cu₂O and β phase show no significant alteration.

The results of antibacterial efficiency against *E. coli* revealed a significant decrease in the killing rate on the laser-treated surfaces in comparison to that on the polished surface. This is firstly attributed to the reduced release of copper concentration on the modified surface. Secondly, it is due to a higher corrosion resistance of zinc rich oxide phases in wet conditions. This property as well as the significantly reduced wettability can be very advantageous in the application of laser structured brass underwater conditions to minimize the material damage e.g., that occurs as a consequence of biofouling. However, this needs to be further investigated in future studies to acquire a full understanding of the corrosion resistance of the structured brass under wet conditions.

To summarize, it is essential to recognize that while the ultrashort pulsed laser was utilized for the surface modification and the HAZ was at the nanoscale, it should not be neglected. The magnitude of chemical alteration profoundly depends on the chemical composition and the phase diagram of the specimen. Furthermore, it is evident that an enhanced antibacterial through contact killing can be achieved with a well-defined topography in combination with a right surface chemistry. In future studies, brass samples with a bulk chemical composition lower than 30 wt.-% can be utilized to investigate the effect of zinc concentration on the formation of oxide and intermetallic phases and hence the resulting influence on antibacterial properties. Other important factors need to be investigated i.e., surface contaminations and wettability to further gain a comprehensive understanding of the bacteria-substrate interaction.

5 Supporting Information

TEM-Electron diffraction images of CuZn37 etched (figure and description); Cu-Zn Phase diagram; Raman bands of CuZn37 samples (table); XPS-based elemental depth profiling (figure and description), XPS-spectra of CuZn37 in O 1s region (figure and description); Results of STM exhibiting the topography (figure)

6 Corresponding Author

Aisha Saddiqa Ahmed - Chair of Functional Materials, Department of Material Science and Engineering, Saarland University, 66123 Saarbrücken, Germany; Email: aisha.ahmed@uni-saarland.de

7 Credit author statement

Aisha S. Ahmed: Conceptualization, Investigation, Validation, Visualization, Writing – original draft; **Daniel W. Müller:** Investigation, Validation, Writing – review & editing; **Stephanie Bruyere:** Investigation, Validation, Writing – review; **Anne Holtsch:**

Investigation, Validation, Writing – review; **Frank Müller**: Investigation, Validation, Writing – review & editing; **Jenifer Barrirero**: Investigation, Validation, Writing – review & editing; **Kristina Brix**: Investigation, Validation, Writing – review; **Sylvie Migots**: Investigation; **Ralf Kautenburger**: Supervision; **Karin Jacobs**: Supervision; **Jean-François Pierson**: Investigation, Validation, Writing – review & editing, Resources, Supervision; **Frank Mücklich**: Funding acquisition, Resources, Supervision

8 Funding

A.A. has been funded by the German Aerospace Center - Space Administration (DLR) within the project “Investigation of antimicrobial metal surfaces under space conditions - An effective strategy to prevent microbial biofilm formation” (project number 50WB1930). D.M. has been funded by the German Research Foundation (DFG) within the project “Controlled bacterial interaction to increase the antimicrobial efficiency of copper surfaces” (project number 415956642). K.J. and A.H. acknowledge support from the German Research Foundation (DFG) via the Collaborative Research Center SFB 1027.

9 Acknowledgement

The Author would like to thank to the group of Prof. Rolf Müller from the Helmholtz Centre of Infection Research in Saarbrücken for providing *E. coli*.

10 Abbreviations

Atom probe tomography (APT), brass with 37% zinc content (CuZn37), confocal laser scanning microscopy (CLSM), colony-forming units (CFU), Dalton or unified atomic mass unit (Da), *Escherichia coli* (*E. coli*), Fast Fourier Transform image (FFT), full width at half maximum (FWHM), grazing incidence X-ray diffraction (GI-XRD), heat affected zone

(HAZ), Vickers hardness (HV), Infrared (IR), local density of electron states (LDOS), phosphate-buffered saline (PBS), polyvinyl chloride (PVC), selected area electron diffraction (SAED), scanning electron microscopy (SEM), scanning transmission electron microscopy along with energy dispersive X-rays spectroscopy (STEM-EDS), scanning tunnel microscopy and spectroscopy (STM and STS), transmission electron microscopy (TEM), ultra short pulsed direct laser interference patterning (USP-DLIP), X-ray photoelectron spectroscopy (XPS).

11 References

- (1) Davies, J. Origins and Evolution of Antibiotic Resistance. *Microbiología (Madrid, Spain)*. 1996, pp 9–16. <https://doi.org/10.1128/membr.00016-10>.
- (2) Hasan, J.; Crawford, R. J.; Ivanova, E. P. Antibacterial Surfaces: The Quest for a New Generation of Biomaterials. *Trends Biotechnol* **2013**, *31* (5), 295–304. <https://doi.org/10.1016/j.tibtech.2013.01.017>.
- (3) Müller, D. W.; Löblein, S.; Terriac, E.; Brix, K.; Siems, K.; Moeller, R.; Kautenburger, R.; Mücklich, F. Increasing Antibacterial Efficiency of Cu Surfaces by Targeted Surface Functionalization via Ultrashort Pulsed Direct Laser Interference Patterning. *Adv Mater Interfaces* **2021**, *8* (5). <https://doi.org/10.1002/admi.202001656>.
- (4) Luo, J.; Ahmed, A.; Pierson, J. F.; Mücklich, F. Tailor the Antibacterial Efficiency of Copper Alloys by Oxidation: When to and When Not To. *J Mater Sci* **2022**, *57* (5), 3807–3821. <https://doi.org/10.1007/s10853-022-06879-5>.
- (5) Rößler, F.; Lang, V.; Günther, D.; Lasagni, A. F. Fabricating Three-Dimensional Periodic Micro Patterns on Photo-Resists Using Laser Interference Lithography. *Adv Eng Mater* **2017**, *19* (5). <https://doi.org/10.1002/adem.201600855>.

- (6) Quirk, T. Insect Wings Shred Bacteria to Pieces. *Nature* **2013**.
<https://doi.org/10.1038/nature.2013.12533>.
- (7) Luís, Â.; Domingues, F.; Ramos, A. Production of Hydrophobic Zein-Based Films Bioinspired by the Lotus Leaf Surface: Characterization and Bioactive Properties. *Microorganisms* **2019**, *7* (8).
<https://doi.org/10.3390/microorganisms7080267>.
- (8) Borda D'Água, R.; Branquinho, R.; Duarte, M. P.; Maurício, E.; Fernando, A. L.; Martins, R.; Fortunato, E. Efficient Coverage of ZnO Nanoparticles on Cotton Fibres for Antibacterial Finishing Using a Rapid and Low Cost: In Situ Synthesis. *New Journal of Chemistry* **2018**, *42* (2), 1052–1060.
<https://doi.org/10.1039/c7nj03418k>.
- (9) Raffi, M.; Mehrwan, S.; Bhatti, T. M.; Akhter, J. I.; Hameed, A.; Yawar, W.; Ul Hasan, M. M. Investigations into the Antibacterial Behavior of Copper Nanoparticles against Escherichia Coli. *Ann Microbiol* **2010**, *60* (1), 75–80.
<https://doi.org/10.1007/s13213-010-0015-6>.
- (10) Lasagni, A. F.; Gachot, C.; Trinh, K. E.; Hans, M.; Rosenkranz, A.; Roch, T.; Eckhardt, S.; Kunze, T.; Bieda, M.; Günther, D.; Lang, V.; Mücklich, F. Direct Laser Interference Patterning, 20 Years of Development: From the Basics to Industrial Applications. In *Laser-based Micro- and Nanoprocessing XI*; SPIE, 2017; Vol. 10092, p 1009211. <https://doi.org/10.1117/12.2252595>.
- (11) Momma, C.; Nolte, S.; Chichkov, B. N.; Alvensleben, F. v; Tunnermann, A. T. *Precise Laser Ablation with Ultrashort Pulses*; 1997; Vol. 109.
- (12) Korte, F.; Serbin, J.; Koch, J.; Egbert, A.; Fallnich, C.; Ostendorf, A.; Chichkov, B. N. Towards Nanostructuring with Femtosecond Laser Pulses. *Appl Phys A Mater Sci Process* **2003**, *77* (2), 229–235. <https://doi.org/10.1007/s00339-003-2110-z>.

- (13) Nolte, S.; Momma, C.; Jacobs, H.; Tünnermann, A.; Chichkov, B. N.; Wellegehausen, B.; Welling, H. Ablation of Metals by Ultrashort Laser Pulses. *Journal of the Optical Society of America B* **1997**, *14* (10), 2716. <https://doi.org/10.1364/JOSAB.14.002716>.
- (14) Sonntag, S.; Roth, J.; Gaehler, F.; Trebin, H. R. Femtosecond Laser Ablation of Aluminium. *Appl Surf Sci* **2009**, *255* (24), 9742–9744. <https://doi.org/10.1016/j.apsusc.2009.04.062>.
- (15) Stark, T.; Alamri, S.; Aguilar-Morales, A. I.; Kiedrowski, T.; Lasagni, A. F. Positive Effect of Laser Structured Surfaces on Tribological Performance. *Journal of Laser Micro Nanoengineering* **2019**, *14* (1), 13–18. <https://doi.org/10.2961/jlmn.2019.01.0003>.
- (16) Rosenkranz, A.; Hans, M.; Gachot, C.; Thome, A.; Bonk, S.; Mücklich, F. Direct Laser Interference Patterning: Tailoring of Contact Area for Frictional and Antibacterial Properties. *Lubricants* **2016**, *4* (1). <https://doi.org/10.3390/lubricants4010002>.
- (17) Roch, T.; Benke, D.; Milles, S.; Roch, A.; Kunze, T.; Lasagni, A. Dependence between Friction of Laser Interference Patterned Carbon and the Thin Film Morphology. *Diam Relat Mater* **2015**, *55*, 16–21. <https://doi.org/10.1016/j.diamond.2015.02.002>.
- (18) Heilmann, S.; Zwahr, C.; Knape, A.; Zschetzsche, J.; Lasagni, A. F.; Füssel, U. Improvement of the Electrical Conductivity between Electrode and Sheet in Spot Welding Process by Direct Laser Interference Patterning. *Adv Eng Mater* **2018**, *20* (6). <https://doi.org/10.1002/adem.201700755>.
- (19) Lutey, A. H. A.; Gemini, L.; Romoli, L.; Lazzini, G.; Fuso, F.; Faucon, M.; Kling, R. Towards Laser-Textured Antibacterial Surfaces. *Sci Rep* **2018**, *8* (1). <https://doi.org/10.1038/s41598-018-28454-2>.

- (20) Aguilar-Morales, A. I.; Alamri, S.; Voisiat, B.; Kunze, T.; Lasagni, A. F. The Role of the Surface Nano-Roughness on the Wettability Performance of Microstructured Metallic Surface Using Direct Laser Interference Patterning. *Materials* **2019**, *12* (7). <https://doi.org/10.3390/ma12172737>.
- (21) Fu, Y.; Soldera, M.; Wang, W.; Milles, S.; Deng, K.; Voisiat, B.; Nielsch, K.; Lasagni, A. F. Wettability Control of Polymeric Microstructures Replicated from Laser-Patterned Stamps. *Sci Rep* **2020**, *10* (1). <https://doi.org/10.1038/s41598-020-79936-1>.
- (22) Müller, D. W.; Holtsch, A.; Löblein, S.; Pauly, C.; Spengler, C.; Grandthyll, S.; Jacobs, K.; Mücklich, F.; Müller, F. In-Depth Investigation of Copper Surface Chemistry Modification by Ultrashort Pulsed Direct Laser Interference Patterning. *Langmuir* **2020**, *36* (45), 13415–13425. <https://doi.org/10.1021/acs.langmuir.0c01625>.
- (23) Raillard, B.; Gouton, L.; Ramos-Moore, E.; Grandthyll, S.; Müller, F.; Mücklich, F. Ablation Effects of Femtosecond Laser Functionalization on Steel Surfaces. *Surf Coat Technol* **2012**, *207*, 102–109. <https://doi.org/10.1016/j.surfcoat.2012.06.023>.
- (24) Zhang, W.; Cheng, G.; Feng, Q.; Cao, L. Femtosecond Laser Machining Characteristics in a Single-Crystal Superalloy. *Rare Metals* **2011**, *30* (SUPPL.1), 639–642. <https://doi.org/10.1007/s12598-011-0362-z>.
- (25) Lang, V.; Roch, T.; Lasagni, A. F. High-Speed Surface Structuring of Polycarbonate Using Direct Laser Interference Patterning: Toward 1 M2 Min–1 Fabrication Speed Barrier. *Adv Eng Mater* **2016**, *18* (8), 1342–1348. <https://doi.org/10.1002/adem.201600173>.
- (26) Prudent, M.; Iabbaden, D.; Bourquard, F.; Reynaud, S.; Lefkir, Y.; Borroto, A.; Pierson, J. F.; Garrelie, F.; Colombier, J. P. High-Density Nanowells Formation

- in Ultrafast Laser-Irradiated Thin Film Metallic Glass. *Nanomicro Lett* **2022**, *14* (1), 1–15. <https://doi.org/10.1007/s40820-022-00850-4>.
- (27) Luo, J.; Hein, C.; Mücklich, F.; Solioz, M. Killing of Bacteria by Copper, Cadmium, and Silver Surfaces Reveals Relevant Physicochemical Parameters. *Biointerphases* **2017**, *12* (2), 020301. <https://doi.org/10.1116/1.4980127>.
- (28) Hans, M.; Támara, J. C.; Mathews, S.; Bax, B.; Hegetschweiler, A.; Kautenburger, R.; Solioz, M.; Mücklich, F. Laser Cladding of Stainless Steel with a Copper-Silver Alloy to Generate Surfaces of High Antimicrobial Activity. *Appl Surf Sci* **2014**, *320*, 195–199. <https://doi.org/10.1016/j.apsusc.2014.09.069>.
- (29) Bieda, M.; Siebold, M.; Lasagni, A. F. Fabrication of Sub-Micron Surface Structures on Copper, Stainless Steel and Titanium Using Picosecond Laser Interference Patterning. *Appl Surf Sci* **2016**, *387*, 175–182. <https://doi.org/10.1016/j.apsusc.2016.06.100>.
- (30) Matias, M. L.; Nunes, D.; Pimentel, A.; Ferreira, S. H.; Borda D'Água, R.; Duarte, M. P.; Fortunato, E.; Martins, R. Paper-Based Nanoplatfoms for Multifunctional Applications. *J Nanomater* **2019**, *2019*. <https://doi.org/10.1155/2019/6501923>.
- (31) Vincent, M.; Duval, R. E.; Hartemann, P.; Engels-Deutsch, M. Contact Killing and Antimicrobial Properties of Copper. *J Appl Microbiol* **2018**, *124* (5), 1032–1046. <https://doi.org/10.1111/jam.13681>.
- (32) Grass, G.; Rensing, C.; Solioz, M. Metallic Copper as an Antimicrobial Surface. *Appl Environ Microbiol* **2011**, *77* (5), 1541–1547. <https://doi.org/10.1128/AEM.02766-10>.
- (33) Meister, T. L.; Fortmann, J.; Breisch, M.; Sengstock, C.; Steinmann, E.; Köller, M.; Pfaender, S.; Ludwig, A. Nanoscale Copper and Silver Thin Film Systems

- Display Differences in Antiviral and Antibacterial Properties. *Sci Rep* **2022**, *12* (1), 1–10. <https://doi.org/10.1038/s41598-022-11212-w>.
- (34) Luo, J.; Hein, C.; Pierson, J. F.; Mücklich, F. Sodium Chloride Assists Copper Release, Enhances Antibacterial Efficiency, and Introduces Atmospheric Corrosion on Copper Surface. *Surfaces and Interfaces* **2020**, *20*. <https://doi.org/10.1016/j.surfin.2020.100630>.
- (35) Nijhout, H. F. Elements of Butterfly Wing Patterns. *Journal of Experimental Zoology* **2001**, *291* (3), 213–225. <https://doi.org/10.1002/jez.1099>.
- (36) Wilson, S. J.; Hutley, M. C. The Optical Properties of ‘Moth Eye’ Antireflection Surfaces. *Opt Acta (Lond)* **1982**, *29* (7), 993–1009. <https://doi.org/10.1080/713820946>.
- (37) Selvaraj, S.; Ponmariappan, S.; Natesan, M.; Palaniswamy, N. Dezincification of Brass and Its Controlan Overview. *Corrosion Reviews* **2003**, *21* (1), 41–74. <https://doi.org/10.1515/CORRREV.2003.21.1.41>.
- (38) Müller, D. W.; Fox, T.; Grützmacher, P. G.; Suarez, S.; Mücklich, F. Applying Ultrashort Pulsed Direct Laser Interference Patterning for Functional Surfaces. *Sci Rep* **2020**, *10* (1). <https://doi.org/10.1038/s41598-020-60592-4>.
- (39) Małag, A. Simple Interference Method of Diffraction Grating Generation for Integrated Optics by the Use of a Fresnel Mirror. *Opt Commun* **1980**, *32* (1), 54–58. [https://doi.org/10.1016/0030-4018\(80\)90313-2](https://doi.org/10.1016/0030-4018(80)90313-2).
- (40) Wang, X. Y.; Riffe, D. M.; Lee, Y. S.; Downer, M. C. Time-Resolved Electron-Temperature Measurement in a Highly Excited Gold Target Using Femtosecond Thermionic Emission. *Phys Rev B* **1994**, *50* (11), 8016–8019. <https://doi.org/10.1103/PhysRevB.50.8016>.
- (41) Kirkwood, S. E.; Tsui, Y. Y.; Fedosejevs, R.; Brantov, A. v.; Bychenkov, V. Y. Experimental and Theoretical Study of Absorption of Femtosecond Laser Pulses

- in Interaction with Solid Copper Targets. *Phys Rev B Condens Matter Mater Phys* **2009**, 79 (14). <https://doi.org/10.1103/PhysRevB.79.144120>.
- (42) Hirayama, Y.; Obara, M. Heat-Affected Zone and Ablation Rate of Copper Ablated with Femtosecond Laser. *J Appl Phys* **2005**, 97 (6). <https://doi.org/10.1063/1.1852692>.
- (43) Anisimov, S. I.; Kapeliovich, B. L.; Perel'man, T. L. Electron Emission from the Metal Surfaces Induced by Ultrashort Lasers Pulses. *Zhurnal Eksperimental'noj i Teoreticheskoy Fiziki* **1974**, 66 (2).
- (44) Chichkov, B. N.; Momma, C.; Nolte, S.; Von Alvensleben, F.; Tünnermann, A. Femtosecond, Picosecond and Nanosecond Laser Ablation of Solids. *Appl Phys A Mater Sci Process* **1996**, 63 (2), 109–115. <https://doi.org/10.1007/BF01567637>.
- (45) Abdelmalek, A.; Bedrane, Z.; Amara, E.-H. Thermal and Non-Thermal Explosion in Metals Ablation by Femtosecond Laser Pulse: Classical Approach of the Two Temperature Model. *J Phys Conf Ser* **2018**, 987, 012012. <https://doi.org/10.1088/1742-6596/987/1/012012>.
- (46) Thompson, K.; Lawrence, D.; Larson, D. J.; Olson, J. D.; Kelly, T. F.; Gorman, B. In Situ Site-Specific Specimen Preparation for Atom Probe Tomography. *Ultramicroscopy* **2007**, 107 (2–3), 131–139. <https://doi.org/10.1016/j.ultramic.2006.06.008>.
- (47) Sanders, E. R. Aseptic Laboratory Techniques: Plating Methods. *Journal of Visualized Experiments* **2012**, No. 63, 1–18. <https://doi.org/10.3791/3064>.
- (48) Fairand, B. P.; Clauer, A. H.; Jung, R. G.; Wilcox, B. A. Quantitative Assessment of Laser-Induced Stress Waves Generated at Confined Surfaces. *Appl Phys Lett* **1974**, 25 (8), 431–433. <https://doi.org/10.1063/1.1655536>.

- (49) Masse, J. E.; Barreau, G. Laser Generation of Stress Waves in Metal. *Surf Coat Technol* **1995**, *70* (2–3), 231–234. [https://doi.org/10.1016/0257-8972\(95\)80020-4](https://doi.org/10.1016/0257-8972(95)80020-4).
- (50) Zhigilei, L. v.; Garrison, B. J. Microscopic Mechanisms of Laser Ablation of Organic Solids in the Thermal and Stress Confinement Irradiation Regimes. *J Appl Phys* **2000**, *88* (3), 1281–1298. <https://doi.org/10.1063/1.373816>.
- (51) Ionin, A. A.; Kudryashov, S. I.; Makarov, S. v.; Levchenko, A. O.; Rudenko, A. A.; Saraeva, I. N.; Zayarny, D. A.; Nathala, C. R.; Husinsky, W. Nanoscale Surface Boiling in Sub-Threshold Damage and above-Threshold Spallation of Bulk Aluminum and Gold by Single Femtosecond Laser Pulses. *Laser Phys Lett* **2016**, *13* (2). <https://doi.org/10.1088/1612-2011/13/2/025603>.
- (52) Zuhlke, C. A.; Anderson, T. P.; Alexander, D. R. Formation of Multiscale Surface Structures on Nickel via above Surface Growth and below Surface Growth Mechanisms Using Femtosecond Laser Pulses. *Opt Express* **2013**, *21* (7), 8460. <https://doi.org/10.1364/oe.21.008460>.
- (53) Leitz, K. H.; Redlingshöer, B.; Reg, Y.; Otto, A.; Schmidt, M. Metal Ablation with Short and Ultrashort Laser Pulses. *Phys Procedia* **2011**, *12* (PART 2), 230–238. <https://doi.org/10.1016/J.PHPRO.2011.03.128>.
- (54) Müller, D. W.; Löblein, S.; Pauly, C.; Briesenick, M.; Kickelbick, G.; Mücklich, F. Multi-Pulse Agglomeration Effects on Ultrashort Pulsed Direct Laser Interference Patterning of Cu. *Appl Surf Sci* **2023**, *611*, 155538. <https://doi.org/10.1016/J.APSUSC.2022.155538>.
- (55) Kirkendall, E. O. Diffusion of Zinc in Alpha Brass. *Trans. Am. Inst. Min. Metall* **1942**, *147*, 104–110.
- (56) Ataya, S.; El-Sayed Seleman, M. M. Microstructure Stability Of CuZn37 Brass. In *14th International Materials Symposium*; 2012.

- (57) Kowalski, M.; Spencer, P. J. Thermodynamic Reevaluation of the Cu-Zn System. *Journal of Phase Equilibria* **1993**, *14* (4), 432–438.
- (58) Hasegawa, M. Ellingham Diagram. *Treatise on Process Metallurgy* **2014**, *1*, 507–516. <https://doi.org/10.1016/B978-0-08-096986-2.00032-1>.
- (59) Lopes, A.; Brodlie, K. Interactive Approaches to Contouring and Isosurfacing for Geovisualization. *Exploring Geovisualization* **2005**, 345–361. <https://doi.org/10.1016/B978-008044531-1/50435-8>.
- (60) Liu, T. H.; Hung, F. Y.; Chen, C. H.; Chen, K. J. Microstructure, Optical, Electrical, and Magnetic Properties of ZnO/CuO Thin Films Prepared Using Two-Stage Magnetron Sputtering and Diffusion Doping Process. *Journal of Materials Science: Materials in Electronics* **2020**, *31* (5), 4017–4026. <https://doi.org/10.1007/s10854-020-02949-z>.
- (61) Feng, Y.; Li, Z.; Liu, H.; Dong, C.; Wang, J.; Kulinich, S. A.; Du, X. Laser-Prepared CuZn Alloy Catalyst for Selective Electrochemical Reduction of CO₂ to Ethylene. *Langmuir* **2018**, *34* (45), 13544–13549. <https://doi.org/10.1021/acs.langmuir.8b02837>.
- (62) Huang, N.; Sun, C.; Zhu, M.; Zhang, B.; Gong, J.; Jiang, X. Microstructure Evolution of Zinc Oxide Films Derived from Dip-Coating Sol-Gel Technique: Formation of Nanorods through Orientation Attachment. *Nanotechnology* **2011**, *22* (26). <https://doi.org/10.1088/0957-4484/22/26/265612>.
- (63) Dhama, R.; Nayek, C.; Thirnal, C.; Murugavel, P. Enhanced Magnetic Properties in Low Doped La_{1-x}Ba_xMnO_{3+δ} (X=0, 0.1 and 0.2) Nanoparticles. *J Magn Mater* **2014**, *364*, 125–128. <https://doi.org/10.1016/j.jmmm.2014.04.010>.

- (64) Kalliomäki, M.; Meisalo, V.; Laisaar, A. High Pressure Transformations in Cuprous Oxide. *physica status solidi (a)* **1979**, *56* (2), K127–K131. <https://doi.org/10.1002/pssa.2210560258>.
- (65) Momot, A.; Amini, M. N.; Reekmans, G.; Lamoen, D.; Partoens, B.; Slocombe, D. R.; Elen, K.; Adriaensens, P.; Hardy, A.; Van Bael, M. K. A Novel Explanation for the Increased Conductivity in Annealed Al-Doped ZnO: An Insight into Migration of Aluminum and Displacement of Zinc. *Physical Chemistry Chemical Physics* **2017**, *19* (40), 27866–27877. <https://doi.org/10.1039/c7cp02936e>.
- (66) Itoh, M. Time-Dependent Power Laws in the Oxidation and Corrosion of Metals and Alloys. *Sci Rep* **2022**, *12* (1). <https://doi.org/10.1038/s41598-022-10748-1>.
- (67) Zhu, Y.; Mimura, K.; Lim, J. W.; Isshiki, M.; Jiang, Q. Brief Review of Oxidation Kinetics of Copper at 350 °C to 1050 °C. *Metall Mater Trans A Phys Metall Mater Sci* **2006**, *37* (4), 1231–1237. <https://doi.org/10.1007/s11661-006-1074-y>.
- (68) Poulston, S.; Parlett, P. M.; Stone, P.; Bowker, M. Surface Oxidation and Reduction of CuO and Cu₂O Studied Using XPS and XAES. *Surface and Interface Analysis* **1996**, *24* (12), 811–820. [https://doi.org/10.1002/\(SICI\)1096-9918\(199611\)24:12<811::AID-SIA191>3.0.CO;2-Z](https://doi.org/10.1002/(SICI)1096-9918(199611)24:12<811::AID-SIA191>3.0.CO;2-Z).
- (69) Barreca, D.; Gasparotto, A.; Tondello, E. CVD Cu₂O and CuO Nanosystems Characterized by XPS. *Surface Science Spectra* **2007**, *14* (1), 41–51. <https://doi.org/10.1116/11.20080701>.
- (70) Schedel-Niedrig, T.; Neisius, T.; Böttger, I.; Kitzelmann, E.; Weinberg, G.; Demuth, D.; Schlögl, R. Copper (Sub)Oxide Formation: A Surface Sensitive Characterization of Model Catalysts. *Physical Chemistry Chemical Physics* **2000**, *2* (10), 2407–2417. <https://doi.org/10.1039/b000253o>.

- (71) Wang, Y.; Lany, S.; Ghanbaja, J.; Fagot-Revurat, Y.; Chen, Y. P.; Soldera, F.; Horwat, D.; Mücklich, F.; Pierson, J. F. Electronic Structures of Cu_2O , Cu_4O_3 , and CuO : A Joint Experimental and Theoretical Study. *Phys Rev B* **2016**, *94* (24), 1–10. <https://doi.org/10.1103/PhysRevB.94.245418>.
- (72) Armelao, L.; Barreca, D.; Bertapelle, M.; Bottaro, G.; Sada, C.; Tondello, E. A Sol–Gel Approach to Nanophasic Copper Oxide Thin Films. *Thin Solid Films* **2003**, *442* (1–2), 48–52. [https://doi.org/10.1016/S0040-6090\(03\)00940-4](https://doi.org/10.1016/S0040-6090(03)00940-4).
- (73) Tobin, J. P.; Hirschwald, W.; Cunningham, J. XPS and XAES Studies of Transient Enhancement of $Cu1$ at CuO Surfaces during Vacuum Outgassing. *Applications of Surface Science* **1983**, *16* (3–4), 441–452. [https://doi.org/10.1016/0378-5963\(83\)90085-5](https://doi.org/10.1016/0378-5963(83)90085-5).
- (74) Wiame, F.; Jasnot, F. R.; Wiatowska, J.; Seyeux, A.; Bertran, F.; le Fèvre, P.; Taleb-Ibrahimi, A.; Maurice, V.; Marcus, P. Oxidation of α -Brass: A Photoelectron Spectroscopy Study. *Surf Sci* **2015**, *641*, 51–59. <https://doi.org/10.1016/j.susc.2015.05.013>.
- (75) Mrowec, S.; Stokłosa, A. Oxidation of Copper at High Temperatures. *Oxidation of Metals* **1971**, *3* (3), 291–311. <https://doi.org/10.1007/BF00603530>.
- (76) Gutmann, S.; Conrad, M.; Wolak, M. A.; Beerbom, M. M.; Schlaf, R. Work Function Measurements on Nano-Crystalline Zinc Oxide Surfaces. *J Appl Phys* **2012**, *111* (12). <https://doi.org/10.1063/1.4729527>.
- (77) Gordon, P. G.; Bačić, G.; Lopinski, G. P.; Barry, S. T. Work Function of Doped Zinc Oxide Films Deposited by ALD. *J Mater Res* **2020**, *35* (7), 756–761. <https://doi.org/10.1557/jmr.2019.334>.
- (78) Mehtar, S.; Wiid, I.; Todorov, S. D. The Antimicrobial Activity of Copper and Copper Alloys against Nosocomial Pathogens and Mycobacterium Tuberculosis Isolated from Healthcare Facilities in the Western Cape: An in-Vitro Study.

Journal of Hospital Infection **2008**, 68 (1), 45–51.

<https://doi.org/10.1016/j.jhin.2007.10.009>.

12 Table of Contents

